CHINESE OPTICS LETTERS

Vol. 23, No. 1 | January 2025

Enhanced reflection laser protection thin films compatible with visible light stealth

Zexiang He (何泽湘)[1,2], Zexiong Hu (胡泽雄)[1,2], Jian Yang (杨 坚)[1,2], Weijie Chen (陈炜杰)[1,2], Zhenzhen Duan (段珍珍)[1,2], Ning Wang (王 宁)[1,2], Dan Wang (王 丹)[1,2], Xiaotan Ji (纪晓锬)[1,2], Nan Chen (陈 楠)[1,2], Zhengqian Luo (罗正钱)[1,2], and Yikun Bu (卜轶坤)[1,2*]

[1] School of Electronic Science and Engineering (National Model Microelectronics College), Xiamen University, Xiamen 361005, China

[2] Fujian Key Laboratory of Ultrafast Laser Technology and Applications, Xiamen University, Xiamen 361005, China

*Corresponding author: buyikun0522@xmu.edu.cn

Received May 30, 2024 | Accepted July 29, 2024 | Posted Online February 18, 2025

For bicolor regulation in laser protection compatible with visible light stealth, a metal–dielectric–enhanced reflection asymmetric Fabry–Perot structure is proposed that has high reflectance at the laser wavelength and the color control of the visible spectrum. The six-layer reflection enhancement unit is composed of an Al metal mirror, SiO_2, Ta_2O_5, and an ultrathin Nb metal layer. The synergistic relationship between the background color and laser wavelength reflectance was analyzed and simulated. Six different colors from blue to red with high reflectance at 1064 nm laser wavelength up to 97.84% were prepared. The thin films can withstand 2535 W cm^{-2} power density continuous irradiation for 60 s without being destroyed. Moreover, a symmetrical structure presents the spectrum consistency from both directions, which makes the potential to be applied to the laser protective coatings. The blue symmetrical microreflector sample was prepared and sprayed on the nonplanar models to demonstrate the actual application effect. This simple and efficient scheme provides an innovative technical approach in the field of surface laser protection.

Keywords: laser protection; visible light stealth; thin films.
DOI: 10.3788/COL202523.012602

1. Introduction

High-power fiber lasers[1] have garnered significant attention in the fields of laser processing[2], laser weaponry[3], and other related domains due to their inherent advantages, such as superior beam quality[4], exceptional conversion efficiency[5], compact size[6], and user-friendly operation[7]. In recent years, high-energy short-range lasers have demonstrated their capability to effectively intercept tactical targets[8] within a limited range[9], rendering them highly destructive for impacted facilities. Consequently, the implementation of efficient safeguards against high-energy laser irradiation is increasingly imperative. Currently, laser protection technology primarily involves lens, window, and detector protection through optical thin films[10–12] and surface protection via metal or ceramic sprayed coatings[13–15]. The two protection types have very distinct application fields and protective effects. Using physical vapor deposition technology, which can control the thickness error within 2%[10], optical thin films can be applied to precision optical components with high laser damage resistance. For example, by adjusting the internal electric field distribution of each material, Nasiri *et al.* designed and manufactured all-dielectric and metal–dielectric mirrors with high laser-induced damage threshold (LIDT) for a continuous wave at 10.6 μm[11]. Instead, metal or ceramic sprayed coatings are surface treatment methods made of granular metal materials such as Al, silver, and gold powder, and ceramic materials such as Ta_2O_5, SiO_2, Ba_2SmTaO_6, etc.[12], which act on large or shaped workpieces in heat- and radiation-resistant scenarios. They are primary applicable strategies for coarse surfaces of military equipment such as aircraft[13]. The substrate treated with spray coatings always shows a lower temperature rise effect on the back side. For example, Xue *et al.* used a coating made of TiO_2 and BN powders with a reflectance of 78.8% at 1064 nm, and the back temperature was 186°C when the laser power density of 1000 W cm^{-2} was continuously irradiated for 10 s[14]. However, further improvement of reflectivity is expected to obtain better antilaser coatings[15]. The current challenge lies in the application of laser-protective optical thin-film technology effectively applied to sprayed coatings, aiming to achieve enhanced reflectivity and resistance against laser damage on equipment surfaces.

Because of the limited hard damage range, laser weapons are usually used in close combat scenes. Visible light stealth[13,16,17]

suitable for close combat is extremely important, which is usually achieved by camouflage technologies, such as multiband compatible stealth by employing Al powder and modified Cr_2O_3 hybrid filler in an IRS coating[13] and whole-infrared-band camouflage with dual-band radiative heat dissipation by constructing seven-layer thin film[16]. The color of the coating primarily originates from the filler, whereas the film achieves controllable color by manipulating its structure. Introducing a Fabry–Perot (FP) cavity on the Al foil, Xiong *et al.* adjusted the parameters of the dielectric layer using different oxidation time and voltages to achieve a variety of colors for visible light stealth[17]. According to the characteristics of short-range laser protection, the research on thin films that possess both visible light stealth and excellent laser protection performance represents a crucial direction for development in the field of laser protection.

In this work, we propose a composite functional thin-film structure featuring compatibility with visible light stealth and laser protection, which is achieved by constructing an enhanced reflection asymmetric FP cavity. Consisting of a metal mirror layer, high-low index dielectrics, and an ultrathin metal layer, the structure can achieve higher reflectivity of laser wavelength while providing multidimensional stealth control mechanisms for achieving colors with varying hues and saturation to cater to diverse environmental requirements. The analysis focused on the synergistic relationship between background color and central wavelength reflectance, utilizing a 1064 nm laser. Finally, six distinct colors from blue to red were designed and prepared with a reflectance of more than 95% at the 1064 nm laser wavelength. The prepared thin films can withstand 2500 W cm^{-2} power density continuous irradiation for 60 s without being destroyed. Moreover, the symmetric thin-film structure applied to laser protective coatings, which has spectral consistency on both sides of the thin film, is proposed and realized. The blue coating is prepared and sprayed on the models to demonstrate the actual effect. This method verifies the feasibility of the functional thin film from theory to practical application.

2. Simulation and Experiments

The evolution of thin-film structure in this paper is shown in Fig. 1(a). The traditional asymmetric FP cavity structure denoted as α, consists of three layers: a metal layer, a dielectric layer, and an ultrathin metal absorbing layer. It exhibits color variation as the thickness of the dielectric changes. The metal–dielectric enhanced reflective film, as β shows, can achieve high reflectance at the center wavelength within a few layers by periodically stacking high and low refractive index dielectric materials on a metal layer. Based on the above structures, we proposed an enhanced reflection type asymmetric FP cavity structure for laser protection thin film with compatible visible light stealth, which is depicted as γ. Due to the thickness of the initial metal layer grown on the substrate exceeding the skin depth of incident light, there is negligible electromagnetic field propagation at the interface between the substrate and the

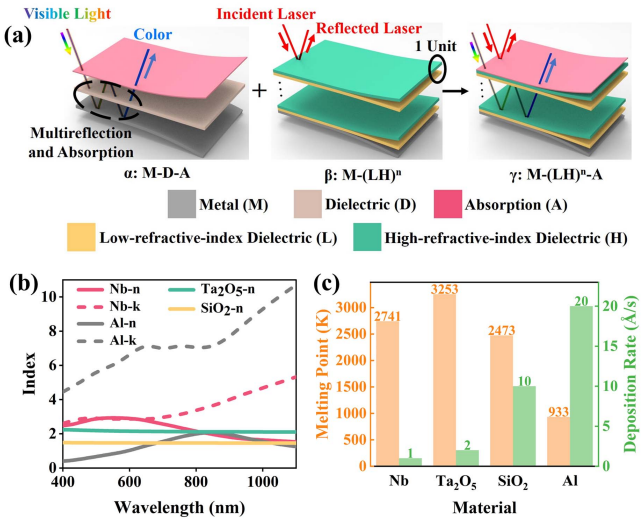

Fig. 1. Structure and parameters of thin films. (a) Diagram of the thin-film structure; (b) optical constants of the materials; (c) melting points and deposition rates.

metal. As a result, subsequent layer growth is equivalent to occurrence on the base of the metal. The optical constants of the materials used in the experiment at the 400–1100 nm band are listed in Fig. 1(b). It should be noted that SiO_2 and Ta_2O_5 exhibit zero absorption coefficients within this wavelength range; hence, they are not depicted. Figure 1(c) presents information on the melting point and appropriate deposition rate for each material. Although being in the innermost part of the film structure, Al possesses a much lower melting point compared to other materials. This can potentially lead to film failure under high-power fiber lasers and must be taken into consideration during film design and preparation.

The spectral characteristics of structure β and γ are identical at the central wavelength, while other bands exhibit distinct absorption effects. By carefully selecting the thickness of the absorbing layer, the structure γ can achieve a high reflectivity for laser wavelength and maintain controllable spectral characteristics within the visible light range. In this study, the thin film employs Al, Nb, and SiO_2 for low refractive index material while Ta_2O_5 for high. Al is more cost-effective and readily available with broadband high reflection compared to silver and gold. The high melting point, chemical stability, and appropriate optical constants of Nb make it suitable as an ultrathin-absorbing layer material exposed to the atmospheric environment[18]. Dielectric films composed of Ta_2O_5 and SiO_2 possess high damage thresholds and a large refractive index contrast ratio. This makes it easier to achieve high reflectivity at the laser wavelength and provides effective laser protection[19]. A change in the optical thickness of dielectrics is illustrated in Fig. 2(a). The color variation of different structures is illustrated in Fig. 2(a), and the reflectance of the central wavelength under different colors is indicated by characters with a standard of no less than 90%. The vertical and horizontal axes represent the thicknesses of SiO_2 and Ta_2O_5, respectively, in quarter-wave optical thickness (QWOT) units of the central wavelength (1064 nm). On the left

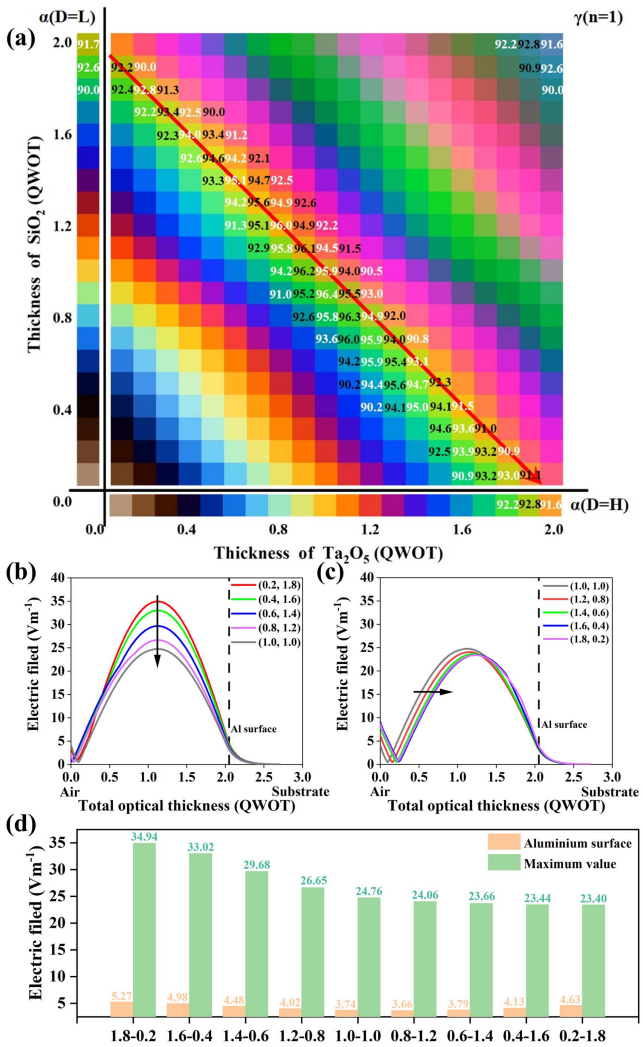

Fig. 2. Color distribution and electric field regulation. (a) The color of the thin films and reflectance at the central wavelength ($\lambda_0 = 1064$ nm) vary by changing the optical thickness of dielectrics. (b)–(c) The electric field intensity distribution changes with the thickness of each dielectric in the same total optical thickness. (d) The maximum and Al layer surface electric field intensity of each film.

side of the vertical axis and below the horizontal axis, color variation is observed with changes in dielectric thickness when SiO_2 and Ta_2O_5 are, respectively, substituted for the dielectric layer in structure α, which are denoted as α (D = L) and α (D = H). The first quadrant region corresponds to the color change observed when altering the thickness of dielectrics on the structure γ with period $n = 1$, which is referred to as γ ($n = 1$). The color exhibited by α (D = L) and α (D = H) undergoes a one-dimensional change as the thickness of the dielectric varies. On the other hand, γ ($n = 1$) features two layers of different dielectrics, enabling a two-dimensional approach to color regulation. This allows for achieving a more diverse and intricate range of colors. The laser reflectance of α (D = L) and α (D = H) does not exceed 93%, while the reflectance of γ ($n = 1$) can surpass 96%. This demonstrates that γ ($n = 1$) effectively enhances laser protection capabilities. For color blocks with equal optical thicknesses in the direction of slope −1 such as the red line in Fig. 2(a), similar colors appear but exhibit slightly different hues. However, the electric field intensity distribution of each film is obviously different, as shown in Figs. 2(b) and 2(c). The marking of the curve corresponds to the coordinates in Fig. 2(a). For example, (0.2, 1.8) indicates that the thicknesses of Ta_2O_5 and SiO_2 layers are 0.2 and 1.8 QWOT, respectively. Figure 2(d) shows the maximum and Al layer surface electric field intensity of each film. Selecting the appropriate dielectric thickness can effectively reduce the electric field intensity inside the film and protect the vulnerable material.

The adjustment of the dielectrics' thickness allows for the attainment of different colors, while a variation in color saturation is brought about by altering the thin Nb layer's thickness. The schematic diagram of γ ($n = 1$) is depicted in Fig. 3(a). Upon incidence of visible light and a 1064 nm laser, the film exhibits reflection properties that achieve both laser protection and visible-light stealth effect according to the designed target color. Under the assumption that the thickness of other materials remains constant, noticeable spectral variations can be observed by altering the thickness of the Nb layer. Figure 3(b) illustrates the spectra of γ ($n = 1$) with Nb thicknesses ranging from 0 to 20 nm in increments of 5 nm. Using the 0 nm sample as a baseline reference, it is evident that introducing a thin layer of Nb induces significant changes in the spectrum. Typically, a 5 nm

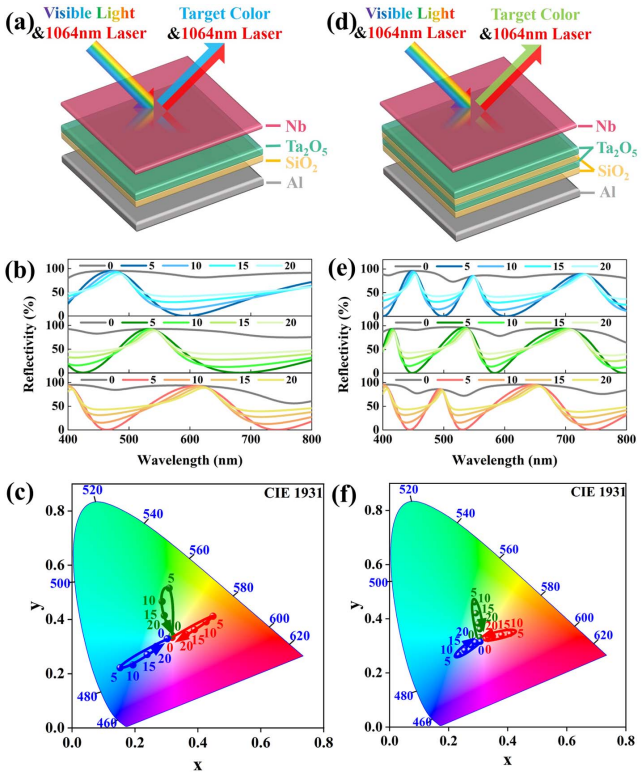

Fig. 3. Characterizations on color saturation control. (a)–(c) Saturation of structure γ ($n = 1$) varies by changing the thickness of the Nb layer; (d)–(f) saturation of structure γ ($n = 2$) varies by changing the thickness of the Nb layer.

layer of Nb yields maximum color saturation. However, as the Nb layer thickness increases beyond this point, there is minimal alteration in film color while saturation gradually diminishes to achieve varying degrees of color intensity. In Fig. 3(c), the CIE 1931 coordinates corresponding to the colors of varying saturation in Fig. 3(b) are indicated, while the arrowed curve illustrates the trend of color coordinate change with increasing Nb layer thickness. Notably, by expanding the period of γ from $n = 1$ to 2, theoretically incorporating an additional pair of high/low refractive index layers, the film can achieve higher central wavelength reflectance and consequently enhance laser protection effectiveness. The color of γ $(n = 2)$ is also investigated, as illustrated in Figs. 3(d)–3(f).

In contrast to γ $(n = 1)$, γ $(n = 2)$ configuration exhibits multiple peaks and troughs within the visible-light spectrum, facilitating the attainment of mixed colors. By transitioning from a two-dimensional to a four-dimensional color space, γ $(n = 2)$ enables the achievement of colors that are challenging with γ $(n = 1)$.

Finally, a set of six color samples ranging from blue to red was prepared in the experiment, as Fig. 4 shows, and the thickness parameters of each sample are shown in Table 1. The fan-shaped sample consisted of Al foil with a wrinkled surface, which is utilized to exhibit the appearance of films with rough surfaces in practical applications. On the other hand, the circular sample comprised a BK7 base and was employed for spectral measurement and laser protection testing purposes. The chromaticity coordinates for each sample and the target value of the design are depicted in Fig. 4(b). Among these samples, sample 1 (S_1) represents a film system structure consisting of γ $(n = 1)$ while sample 3 (S_3) corresponds to γ $(n = 2)$. Further testing and analysis have been conducted on both S_1 and S_3.

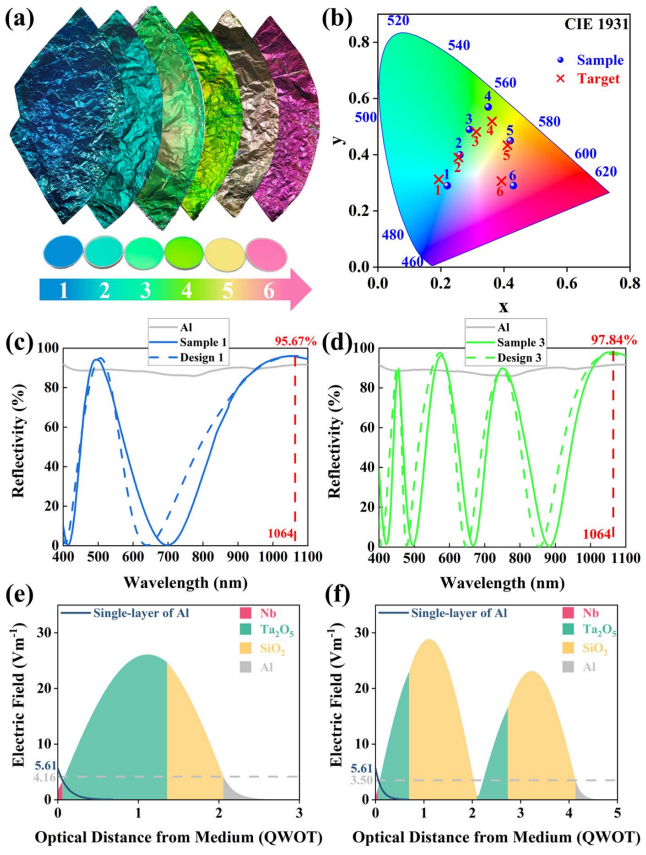

Fig. 4. Preparation of different samples. (a) Samples on Al foil and BK7 substrates; (b) chromaticity coordinates of samples; (c) measurement and design spectra of S_1; (d) measurement and design spectra of S_3; electric field distributions of (e) S_1 and (f) S_3 at the wavelength of 1064 nm.

Table 1. Parameters of Different Samples.

	1	2	3	4	5	6
Al (nm)	100	100	100	100	100	100
SiO_2 (nm)	91	193	222	178	243	272
Ta_2O_5 (nm)	152	80	56	117	84	79
SiO_2 (nm)		162	244			252
Ta_2O_5 (nm)		143	94			109
Nb (nm)	5	5	5	6	10	10

With more than 95%, the reflectance of S_1 and S_3 at the wavelength of 1064 nm is higher than that of a reference single-layer Al with a thickness of 100 nm, as shown in Figs. 4(c) and 4(d). Furthermore, the design spectra match well with the measurement spectra. The slight spectral redshift is attributed to the thickness error in film preparation and the measurement deviation. As shown in Figs. 4(e) and 4(f), both S_1 and S_3 effectively reduce the surface electric field intensity of Al from an initial value of 5.61 V m^{-1} to values of 4.16 and 3.50 V m^{-1}, respectively, thereby providing enhanced protection for the Al layer, which possesses the lowest melting point.

In practical applications, devices are typically damaged when the protected substrate surface is irradiated after penetrating the protective films or coatings. To simulate real-world scenarios, our testing scheme deviates from measuring the laser-induced damage threshold and instead employs a method involving 1064 nm continuous laser breakdown of films. The measurement data includes laser power density, irradiation time, and spot ablation size. As depicted in Fig. 5, the expanded and collimated 1064 nm laser beam is split into two parts using a beam-splitting mirror: one with low energy and another with high. The low-energy beam is utilized to measure spot size and power density, while the high-energy beam impacts the BK7 sample surface. The sample is placed on a platform with a hollowed-out center. When a breakdown occurs, an energy meter positioned behind the sample platform detects the received energy. Our test utilizes an adjustable 0–20 W 1064 nm continuous fiber laser with a focused spot diameter of 0.8 mm, capable of reaching maximum power density of up to 3800 W cm^{-2}.

The experiment involved measuring the time taken to break down the film by irradiating the sample with varying power densities of the laser. Following fitting, P_0 is defined as the unbroken

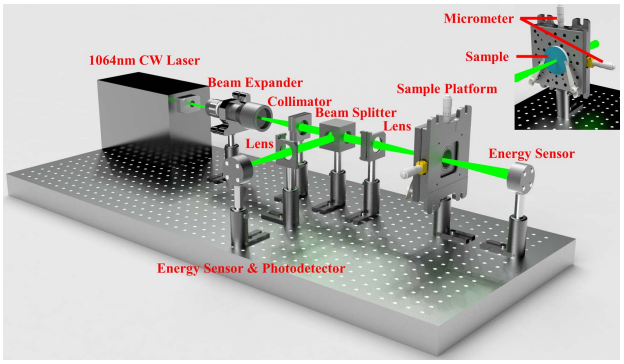

Fig. 5. Schematic diagram of a laser testing device.

power density after 60 s of irradiation, while P_1 is the instantaneous broken power density. Subsequently, starting from 0, the laser was incrementally increased to P_0 at a rate of 50 W cm^{-2} s^{-1} for pretreatment purposes[20]. Then, under different power densities, the breakdown probability after 60 s of irradiation was measured and recorded as P_2 and P_3 for points with probabilities of 0% and 100%, respectively. Figure 6(a) illustrates the laser irradiation test data of the single-layer 100 nm Al sample along with the fitted trend line. The measurement findings indicate that under irradiation of 1237 W cm^{-2}, the single-layer Al remains intact for a duration of 60 s and can be enhanced to 1469 W cm^{-2} after undergoing laser pretreatment. However, even after laser pretreatment, when the laser power density reaches $P_1(\mathrm{Al}) = 1622$ W cm^{-2}, there is still a probability exceeding 80% for breakdown occurrence in single-layer Al. Correspondingly, the laser irradiation test curve of S_1 is shown in Fig. 6(b), with P_0 (S_1) at 2535 W cm^{-2} and P_2 (S_1) increasing to 2600 W cm^{-2}. It should be noted that the breakdown

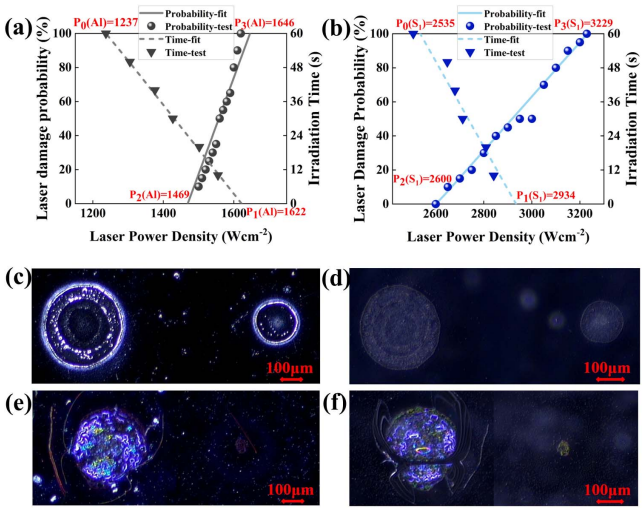

Fig. 6. Laser irradiation test results. (a) Test curve of laser irradiation on single-layer Al; (b) test curve of laser irradiation on S_1; (c) single-layer Al micrograph of the front after irradiation; (d) S_1 micrograph of the front after irradiation; (e) single-layer Al micrograph of the back after irradiation; (f) S_1 micrograph of the back after irradiation.

probability of the S_1 at 2934 W cm^{-2} is reduced to less than 60% after pretreatment. The laser pretreatment process enhances the lower limit of laser protection ability for single-layer Al by effectively reducing surface impurities and minimizing absorption. However, when exposed to higher power density, single-layer Al undergoes melting and expansion, leading to surface flatness damage, further amplifying absorption, and creating a positive feedback loop. In contrast, since S_1 is stacked with dielectric layers that possess a certain porosity, it allows room for Al expansion without affecting the film system's surface topography, thereby significantly improving its laser protection ability.

The micrographs of the front and back of the single-layer Al sample and S_1 after laser irradiation are shown in Figs. 6(c)–6(f). Among them, the large hole represents test points without laser pretreatment, exhibiting varying degrees of ring-shaped irradiation traces or crack damage. The small hole represents a test point after laser pretreatment, demonstrating that laser pretreatment effectively reduces the damaged area, particularly in the case of S_1. Due to the limitations of the instrument, no obvious damage was captured by the eyes or optical microscope even after irradiation of S_3 for 60 s at a maximum power density.

In the series of scanning electron microscope (SEM) images, Fig. 7(a) depicts the surface morphology of crack damage on the large hole shown in Fig. 6(d), exhibiting black patches indicative of impurities or ablative marks near the crack. Conversely, Fig. 7(b) illustrates specific characteristics of the small hole of S_1 in Fig. 6(d), displaying a regular ablative area with fewer surrounding black patches. Through comparison, it is evident that laser pretreatment effectively reduces the damaged area and yields more regular morphological features. Furthermore, Fig. 7(c) showcases ablation marks on S_1 after laser pretreatment without breakdown, representing significantly smaller irradiation traces. Additionally, Figs. 7(e) and 7(f) separately depict sections of S_3 before and after irradiation for 60 s, with the highest power density during the experiment. It can be observed that the initial damage occurs in Al, despite the smooth surface, as shown in Fig. 7(d). Subsequently, molten Al infiltrates into the pores of

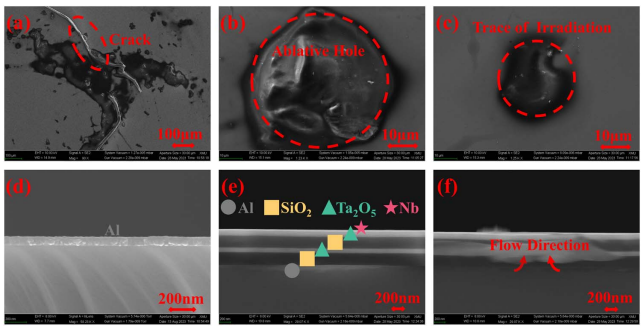

Fig. 7. Series of SEM images. (a) Surface morphology of S_1 exhibiting crack damage; (b) surface morphology of S_1 exhibiting an ablative hole. (c) Surface morphology of S_1 exhibiting a trace of irradiation under an unbroken test. (d) Cross section of 100 nm single-layer Al; (e) cross section of S_3; (f) cross section of S_3 irradiated with the highest power density laser for 60 s.

the dielectric layers without compromising surface flatness, thereby facilitating laser protection.

The conversion from thin film to coating is the key point to the practical application of laser-protective films on irregular surfaces. To realize this conversion, the symmetric thin-film structure based on an asymmetric FP cavity is proposed. This structure ensures the spectral consistency of the microreflectors formed after the film is fragmented. Regardless of which side the light incident originates from during the irradiation process, the same spectral modulation effect can be attained.

The schematic diagram of the film layer plated on the BK7 substrate after achieving S_1 structure symmetry is shown in Fig. 8(a). The front light enters the film layer from the air side and ultimately obtains its spectrum on the air side. On the other hand, the back light passes through a 2 mm thick BK7 base when an incident from the air before reaching the surface of the film layer. The reflected light is then received through the substrate into the air, with additional Fresnel reflection occurring at BK7, resulting in certain differences in both front side and back side spectra. In Fig. 8(b), blue and red lines, respectively, represent the front reflection spectrum and back reflection spectrum. The dashed line represents the simulation design curve while the solid line represents the sample test curve. Figure 8(c) illustrates two sides of colors of the symmetric structure under the BK7 base, where letters F and B denote the front and back sides of the sample, respectively. Although there is a minimal color difference between both sides, the back side exhibits two different images due to the Fresnel reflection effect. Figure 8(d) displays an SEM cross-sectional image showing good symmetry on both sides of Al, which are symmetrical about the Al layer itself. Based on the symmetric structure, film stripping material is plated between BK7 and Nb layer near BK7 to obtain microreflectors that can be further converted into coatings, as Fig. 8(e) shows. By spraying coatings on car models, it can be observed that the base color has minimal impact on the sprayed color shown in Fig. 8(f), indicating that the coating material can be applied to surfaces of any color and shape.

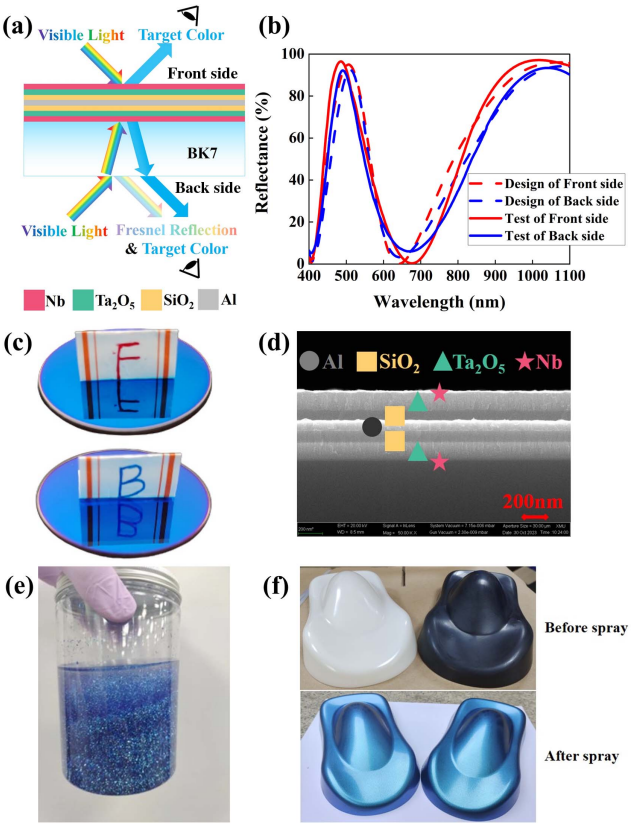

Fig. 8. Verification and application of thin films with symmetrical structure. (a) Schematic diagram of symmetrical S_1 structure on the base; (b) front side and back side spectra of symmetrical S_1; (c) colors of front side and back side. (d) cross section of symmetrical S_1; (e) collection of S_1 microreflectors; (f) coating spraying effect.

3. Conclusion

In summary, the enhanced reflection asymmetric FP cavity structure combines the high reflection from the metal–dielectric enhanced structure and color control of the traditional asymmetric FP cavity. The color control is accompanied by an optimization of the electric field distribution within the film, considering the material characteristics. To replicate the actual application environment, the laser test scheme for breakdown measurement is employed in this experiment. Compared to a 100 nm single-layer Al reference, the power density of S_1 experiencing breakdown after 60 s of irradiation increased from 1237 to 2535 W cm^{-2}. Additionally, the power density with zero probability of breakdown after 60 s of continuous irradiation following laser pretreatment increased from 1469 to 2600 W cm^{-2}. Moreover, the laser pretreatment process is capable of effectively reducing the damaged area. Finally, the symmetric structure thin film was designed and prepared with a good agreement between the spectra obtained from both the front and back sides. Due to the color adjustability of the thin film and coating, this structure can be applied to laser protection scenes in various background color environments and provides a new method for the future laser protection field.

Acknowledgements

This work was supported by the National Natural Science Foundation of China (No. 62375231), the National Key Research and Development Program of China (No. 2020YFC2200403), and the Fujian Province Science and Technology Planning Project of China (No. 2022H6015). The authors thank the School of Electronic Science and Engineering (National Model Microelectronics College), Xiamen University, for equipment support.

References

1. A. Klenke, C. Jauregui, A. Steinkopff, *et al.*, "High-power multicore fiber laser systems," Prog. Quantum Electron. **84**, 100412 (2022).

2. X. S. Jia, Y. Q. Chen, L. Liu, *et al.*, "Combined pulse laser: reliable tool for high-quality, high-efficiency material processing," Opt. Laser Technol. **153**, 108209 (2022).
3. J. Cook, "High-energy laser weapons since the early 1960s," Opt. Eng. **52**, 021007 (2013).
4. J. Ballato, P. D. Dragic, and M. J. F. Digonnet, "Prospects and challenges for all-optical thermal management of fiber lasers," J. Phys. D **57**, 162001 (2024).
5. L. Zhang, Y. D. Guo, Z. Z. Chen, *et al.*, "A near 60% efficiency single-slab Nd: YAG high-power laser with adjustable pulse duration," IEEE Photon. Technol. Lett. **31**, 405 (2019).
6. G. V. Burkovsky, A. S. Boreysho, A. V. Fedin, *et al.*, "High-energy compact-size diode-pumped Nd:YAG laser with self-pumped phase-conjugate dynamic cavity," in *International Conference Laser Optics (LO)* (IEEE, 2016).
7. R. A. Sacks, K. P. McCandless, E. Feigenbaum, *et al.*, "The virtual beamline (VBL) laser simulation code," in *3rd Biennial Conference on High Power Lasers for Fusion Research* (SPIE-International Society of Optical Engineering, 2015).
8. F. Teng, X. P. Guo, Y. F. Song, *et al.*, "An air target tactical intention recognition model based on bidirectional GRU with attention mechanism," IEEE Access **9**, 169122 (2021).
9. J. Wan, "Damage effect evaluation of laser weapon system," in *2nd Symposium on Novel Technology of X-Ray Imaging* (SPIE-International Society of Optical Engineering, 2018).
10. Y.-L. Chen and P.-J. Wang, "Study of ion-assisted e-beam evaporation coating process on chirped mirrors," Coatings **13**, 356 (2023).
11. Z. Nasiri, H. Fallah, M. Hajimahmoodzadeh, *et al.*, "Investigation of the laser induced damage thresholds of all-dielectric and metal-dielectric mirrors for a continuous wave at 10.6 μm," Opt. Mater. **114**, 110936 (2021).
12. J. Zheng, Z. Ma, Y. Liu, *et al.*, "Thermal damage and ablation behavior of plasma sprayed Ba_2SmTaO_6 coatings irradiated by high power continuous laser," Prog. Nat. Sci. Mater. Int. **31**, 609 (2021).
13. X. Chai, D. Zhu, Q. Chen, *et al.*, "Tailored composition of low emissivity top layer for lightweight visible light-infrared-radar multiband compatible stealth coating," Adv. Compos. Hybrid Mater. **5**, 3094 (2022).
14. X. Y. Xue, Y. X. Peng, J. Huang, *et al.*, "Design and preparation of resin matrix composite coating with good ablation resistance performance under high-energy laser irradiation," Ceram. Int. **49**, 18962 (2023).
15. C. Ma, Z. Ma, L. Gao, *et al.*, "Toward improving the reflectivity of ablative heat-insulating coating under high-energy laser irradiation," J. Mater. Sci. **55**, 15787 (2020).
16. B. Qin, Y. N. Zhu, Y. W. Zhou, *et al.*, "Whole-infrared-band camouflage with dual-band radiative heat dissipation," Light Sci. Appl. **12**, 11 (2023).
17. Y. Xiong, Y. Zhou, J. Tian, *et al.*, "Scalable, color-matched, flexible plasmonic film for visible–infrared compatible camouflage," Adv. Sci. **10**, 2303452 (2023).
18. R. K. Williams, W. H. Butler, R. S. Graves, *et al.*, "Experimental and theoretical evaluation of the phonon thermal conductivity of niobium at intermediate temperatures," Phys. Rev. B **28**, 6316 (1983).
19. C. Xu, H. Dong, J. Ma, *et al.*, "Influences of SiO_2 protective layers and annealing on the laser-induced damage threshold of Ta_2O_5 films," Chin. Opt. Lett. **6**, 228 (2008).
20. H. W. Wang, Q. Chen, Y. P. Yao, *et al.*, "Influence of surface preprocessing on 4H-SiC wafer slicing by using ultrafast laser," Crystals **13**, 15 (2023).